Soft Phonon Modes from Off-center Ge atoms Lead to Ultralow Thermal Conductivity and Superior Thermoelectric Performance in n-type PbSe-GeSe

Journal:	*Energy & Environmental Science*
Manuscript ID	EE-ART-06-2018-001755.R1
Article Type:	Paper
Date Submitted by the Author:	26-Jul-2018
Complete List of Authors:	Luo, Zhongzhen; Nanyang Technological University, MSE 50 Nanyang Avenue; Northwestern University, Department of Chemistry Hao, Shiqiang; Northwestern University, Department of Materials Science and Engineering Zhang, Xiaomi; Northwestern University, Department of Materials Science and Engineering Hua, Xia; Northwestern University, Department of Materials Science and Engineering Cai, Songting; Northwestern University, Department of Materials Science and Engineering Tan, Gangjian; Northwestern University, Department of Chemistry Bailey, Trevor; University of Michigan, Department of Physics Ma, Runchu; University of Michigan, Department of Physics Uher, Ctirad; University of Michigan, Department of Physics Wolverton, Chris; Northwestern University, Department of Materials Science and Engineering Dravid, Vinayak; Northwestern University, Materials Science & Engineering Yan, Qingyu; Nanyang Technological University, MSE Kanatzidis, Mercouri; Northwestern University, Department of Chemistry

Soft Phonon Modes from Off-center Ge atoms Lead to Ultralow Thermal Conductivity and Superior Thermoelectric Performance in n-type PbSe-GeSe

Zhong-Zhen Luo,[1,2] Shiqiang Hao,[3] Xiaomi Zhang,[3] Xia Hua,[3] Songting Cai,[2,3] Gangjian Tan,[2] Trevor P. Bailey,[4] Runchu Ma,[4] Ctirad Uher,[4] Chris Wolverton,[3] Vinayak P. Dravid,[3] Qingyu Yan,[1,*] Mercouri G. Kanatzidis[2,*]

[1]School of Materials Science and Engineering, Nanyang Technological University, 50 Nanyang Avenue 639798, Singapore

[2]Department of Chemistry, Northwestern University, Evanston, Illinois 60208, United States

[3]Department of Materials Science and Engineering, Northwestern University, Evanston, Illinois 60208, United States

[4]Department of Physics, University of Michigan, Ann Arbor, Michigan 48109, United States

ABSTRACT

Historically PbSe has underperformed PbTe in thermoelectric efficiency and has been regarded as an inferior relative to its telluride congener. However, the fifty-fold greater natural abundance of Se relative to Te makes PbSe appealing as a thermoelectric material. We report that the n-type GeSe-alloyed PbSe system achieves a peak figure of merit, *ZT*, of ~1.54 at 773 K and maintains *ZT* values above 1.2 over a broad temperature range from 623 K to 923 K. The highest performing composition is Sb-doped PbSe-12%GeSe, which exhibits an ultralow lattice thermal conductivity of ~0.36 $Wm^{-1}K^{-1}$ at 573 K, close to the limit of amorphous PbSe. Theoretical studies reveal that the alloyed Ge^{2+} atoms prefer to stay at off-center lattice positions, inducing low frequency modes. The Ge atoms also cause the unexpected behavior where the next nearest atom neighbors (6 Pb atoms) oscillate at lower frequencies than in pure PbSe leading to a large reduction of the Debye temperature and acoustic phonon velocity. The $Pb_{0.9955}Sb_{0.0045}Se$-12%GeSe system also shows Ge-rich precipitates and many aligned dislocations within its microstructure which also contribute to phonon scattering. The resultant average *ZT* (ZT_{avg}), a broad measure of the materials potential for functional thermoelectric modules, is 1.06 from 400 K to 800 K, the highest among all previously reported n- and p-type PbSe. This value matches or exceeds even those

of the best n-type PbTe-based thermoelectric materials.

1. INTRODUCTION

Thermoelectric materials are capable of direct solid state conversion of heat to electricity without moving parts or gas emissions, and show a great potential for increasing energy utilization efficiency and reducing greenhouse gas emissions. The efficiency of a thermoelectric material is characterized by the dimensionless figure of merit $ZT = S^2\sigma T/(\kappa_{lat} + \kappa_{ele})$, where S is the Seebeck coefficient, σ is the electrical conductivity, T is the operating temperature, and κ_{lat} and κ_{ele} are the lattice thermal conductivity and charge carrier thermal conductivity, respectively.[1] High ZT is desired for good thermoelectric materials, which can be achieved from large power factors ($PF = S^2\sigma$) and low thermal conductivities. However, except for κ_{lat}, the S, σ, and κ_{ele} are strongly coupled and cannot easily be independently optimized. Strategies to increase the power factor include electronic band structure modification, such as multiple band convergence,[2-5] endotaxial second phase band alignment,[6-9] resonant levels,[10-13] etc. Strategies to reduce κ_{lat} involve hierarchical architectures on all length scales, including alloy scattering (*i.e.*, making solid solutions)[1, 6, 14-24]. In addition, the power generation efficiency (η) of thermoelectric devices is directly dependent on the average figure of merit ZT_{avg} as $\eta = [(T_H - T_C)/T_H]\ [(1 + ZT_{avg})^{1/2} - 1]/[(1 + ZT_{avg})^{1/2} + T_C/T_H]$, where T_H is the hot side temperature and T_C is the cold side temperature. Considering that medium-temperature waste heat sources (*e.g.* from 573 K to 873 K) account for about 90% of all waste heat in the USA,[25] it is important to explore materials with high ZT values and especially ZT_{avg} in the intermediate temperature range because high performance materials in this range are few.

PbTe-based materials with a simple face-centered cubic rock salt structure have outstanding thermoelectric performance and have been extensively studied in both p- and n-type varieties.[15, 26, 27] Nevertheless, the scalable application of PbTe is limited in part because the scarcity of Te in the Earth's crust (only 1/50 the amount of Se). Its sister compound PbSe is less expensive and has many of the attractive features of PbTe, but offers additional advantages such as higher melting point and operation temperatures, however, historically its relative performance has significantly lagged.[28, 29] Theoretical work has suggested that properly hole-doped PbSe can potentially reach ZT close to 2 at 1000 K.[30]

Therefore, PbSe has thus aroused considerable attention as an alternative intermediate temperature thermoelectric material. As a result, there has been substantial progress in enhancing the thermoelectric properties of p-type PbSe in recent years.[8, 31, 32] In contrast, n-type PbSe has much lower performance and its power factor is much more difficult to improve by electronic band structure engineering due to the absence of second band in contrast to the p-type counterpart which feature two closely lying valence bands. Therefore, decreasing κ_{lat} by selectively intensifying the phonon scattering should be the primary strategy of improving the thermoelectric performance of n-type PbSe. Although progress has been achieved, such as $(PbSe)_{0.88}(PbS)_{0.12}$-0.3%$PbCl_2$ (ZT ~1.3 at 900 K),[33] $PbSeAl_{0.01}$ (ZT ~1.3 at 850 K),[34] $Pb_{1.002}Se_{1-x}Br_x$ (ZT ~1.2 at 850 K),[35] the ZT_{avg} values are still relatively low, mainly due to the fact that the ZT value increases steeply only at elevated temperatures. Additional advances are needed as to date there is no report for n-type PbSe-based thermoelectric materials with $ZT_{avg} \geq 1$ in the intermediate temperature range (*e.g.* 300 K to 900 K). Recently, a theoretical study suggested that GeSe can exhibit good charge transport and an ultralow κ_{lat} (below 0.2 $Wm^{-1}K^{-1}$ at 800 K).[36] Thus, we hypothesized that a promising approach to enhance the thermoelectric performance of n-type PbSe could be via GeSe alloying, which had not been previously explored.

Here, we report the preparation of GeSe-alloyed n-type PbSe materials *via* the vacuum melting method combined with subsequent spark plasma sintering (SPS) process. We used Sb as the electron dopant to tune the carrier concentration (n) by substituting Sb^{3+} for Pb^{2+} as a means of optimizing the electronic transport properties of the PbSe matrix. Using first-principles theoretical studies, we find a striking new insight, that alloyed Ge atoms not only exhibit unusually low frequency optical vibrations, but also cause the next six nearest neighbor Pb atoms to oscillate at lower than their normal frequencies. Moreover, Ge-rich nanoscale precipitates as well as lattice and grain boundary dislocations are also observed. As a result, a surprisingly low lattice thermal conductivity is obtained for n-type $Pb_{0.9955}Sb_{0.0045}Se$-12%GeSe which achieves a maximum ZT of 1.54 at 773 K and a ZT_{avg} of 1.14 from 400 K to 900 K, which is the highest for n-type PbSe reported so far.[33, 34, 37-39] Given the historical underperformance of PbSe compared to PbTe-based materials the results

reported here are a milestone since *ZT* matches or exceeds those of the best n-type PbTe-based systems.[4, 20, 40-42] This makes the n-type PbSe-GeSe system promising for thermoelectric generators in the intermediate temperature range.

2. Experimental Section

Synthesis. The starting materials used were Pb wire (99.99%, American Elements, USA), Se shot (99.999%, 5 N Plus, Canada), Sb shot (99.999%, American Elements, USA), and Ge lump (99.999%, Plasmaterials, USA). Ingots were synthesized according to the nominal compositions of $Pb_{0.9955}Sb_{0.0045}Se$-x%GeSe (x = 0, 3, 6, 9, 12 and 14) by first mixing the high-purity starting materials in 13 mm diameter quartz tubes. The Sb-free PbSe-x%GeSe (x = 0, 3, 6, 9, 12 and 14) compounds (~3 g in mass for each, x = 0, 3, 6, 9, 12 and 14, in mole ratio) were synthesized for optical band gap measurements. The tubes were then evacuated to a pressure of ~2×10^{-3} torr then flame-sealed. The raw materials inside the quartz tube were slowly heated to 1473 K over 12 h and soaked at this temperature for 6 h, then furnace cooled to room temperature. For a typical experiment the following amounts were used: Pb (10 g, 48.26 mmol), Se (4.3527 g, 55.13 mmol), Sb (0.0302 g, 0.25 mmol), and Ge (0.4805 g, 6.61 mmol) to prepare a ~15 g ingot of $Pb_{0.9955}Sb_{0.0045}Se$-12%GeSe.

Spark Plasma Sintering (SPS). For SPS processing, the obtained ingots of $Pb_{0.9955}Sb_{0.0045}Se$-x%GeSe were hand ground to a powder using a mechanical mortar and pestle to reduce the grain size to < 53 μm. These powders were subsequently densified by using the SPS technique (SPS-211LX, Fuji Electronic Industrial Co. Ltd.) at 923 K for 10 min in a 12.7 mm diameter graphite die under an axial compressive stress of 40 MPa under vacuum. The manipulations for the powder grinding and charging into graphite die were carried out in a glovebox with a purified N_2 atmosphere. Disk-shaped pellets with thickness of ~10 mm and relative densities > 97% (Table S1, Supporting Information) were obtained. Then the SPS processed samples were annealed at 923 K over 5 h and cooled to room temperature in 5 h; this annealing treatment was repeated three times.

Powder X-ray Diffraction Characterization. Powder X-ray diffraction (PXRD) patterns were recorded from finely ground powders of $Pb_{0.9955}Sb_{0.0045}Se$-x%GeSe samples using a Rigaku Miniflex powder X-ray diffractometer with Ni-filtered Cu K_α (λ = 1.5418 Å) radiation

operating at 40 kV and 15 mA. The scanning range of 2θ was 20 – 80°, and the scan increment was 0.02°. The lattice parameters of all samples were calculated by the Rietveld refinement method.

Band Gap Measurements. Room temperature infrared diffuse reflectance spectra of PbSe-x%GeSe (x = 0, 3, 6, 9, 12 and 14) were taken on finely ground powders to probe the optical energy gap. These samples were undoped to avoid spectroscopic interference from free carriers. The spectra were collected in the mid-IR range (6000 − 400 cm^{-1}) with a Nicolet 6700 FTIR spectrometer at room temperature. The band gaps were converted from reflectance spectra using Kubelka-Munk equations: $\alpha/S' = (1 - R)^2/(2R)$, where R is the reflectance coefficient, α is the absorption coefficient, and S' is the scattering coefficient.[43]

Electrical Transport Properties. An Ulvac Riko ZEM-3 system was used to simultaneously determine the electrical conductivity and Seebeck coefficient under a low-pressure helium atmosphere from 300 K to 923 K. The obtained SPSed pellets were cut into bars, with approximately dimensions of 11 mm × 3 mm × 3 mm. The bars were spray coated with a thin layer (0.1 − 0.2 mm) of boron nitride to avoid evaporation of Se and to protect the instruments. To demonstrate the thermal stability and property reversibility, multiple thermal cycles were performed for both electrical conductivity and Seebeck coefficient. The uncertainties of the Seebeck coe ·cient and electrical conductivity measurements are about 3% and 5%, respectively.[44]

Hall Measurements. The temperature-dependent Hall effect measurement was completed with an AC 4-probe method in a homemade system with excitation fields of ± 0.5 Tesla. The specimens were polished with the size of ~1 mm × 3 mm × 8 mm. The homemade system uses an air-bore, helium-cooled superconducting magnet to generate the field within a high temperature oven that surrounds the Ar-filled sample probe. The estimated error is based on the standard deviation of several data points at a single temperature. The carrier concentration was calculated from the Hall coefficient assuming a single carrier, *i.e.* $n = 1/(e|R_H|)$, where e is the electron charge and R_H is the Hall coefficient, with the error propagated from the Hall coefficient. The Hall mobility (μ_H) was determined as $\mu_H = \sigma R_H$.

Thermal Conductivity. The thermal di ·usivity (D) was measured using the laser flash

analysis method (Netzsch LFA457) under a continuous nitrogen flow in the temperature range 300 K to 923 K. The data was analyzed using a Cowan model with pulse correction. The SPSed pellets were cut and polished into a squared shape of approximately 10 × 10 × 2 mm^3, then coated with a thin layer of graphite to minimize errors from the emissivity of the material. In order to verify the repeatability of D, the measurement was performed for both heating and cooling cycles. The thermal conductivity was calculated with the relationship of $\kappa = D \cdot C_p \cdot \rho$, where C_p is the specific heat capacity (calculated by the formula C_p (per unit mass) = $0.170778 + 2.648764 \times 10^{-5} \times T(/K)$ J $g^{-1}K^{-1}$)[39, 45] and ρ is the density (calculated using the dimensions and mass of each sample). Considering the uncertainties from D (5%), C_p (15%) and ρ (5%), the combined uncertainty for all measurements involved in the determination of ZT is ~20%.

Electron Microscopy. Scanning/Transmission Electron Microscopy (S/TEM) experiments were performed for the $Pb_{0.9955}Sb_{0.0045}Se$-12%GeSe sample. Conventional and high-resolution TEM, selected area electron diffraction (SAED), annular dark field (ADF) STEM imaging and energy dispersive X-ray spectroscopy (EDS) were carried out with a JEOL ARM300F GrandARM TEM operated under 300 kV. The TEM specimen was prepared with conventional methods, including dicing, grinding, dimpling, followed by high energy (2.8 keV) Ar ion milling until hole formation and cleaned with 2 keV and then low energy (300 eV) Ar ion milling. Ar ion milling was performed with a Fischione Model 1050 TEM Mill at cryogenic temperature with the help of a liquid nitrogen cooling stage.

Electronic Band Structure Calculations. Density Functional Theory (DFT)[46, 47] band structure calculations were carried out for pure stoichiometric PbSe and Ge-doped PbSe using a 54-atom supercell. Considering that the dopant Sb atoms only serve for carrier concentration adjustment, we do not include Sb atoms in the supercell. The calculations were performed using the Vienna ab initio Simulation Package (VASP)[48-51] with projector augmented wave pseudopotentials utilizing the generalized gradient approximation and Perdew-Burke-Ernzerhof (PBE) exchange-correlation[52]. For Pb and Ge atoms, the semi core d electrons were treated as valence states. Both relaxation calculations and band structure calculations were performed with a plane-wave basis cutoff energy of 520 eV and spin-orbit

coupling (SOC). The total energies were converged within 0.01 meV with a Monkhorst-Pack k-mesh with 5000 k-points per reciprocal atom in the Brillouin zone.

DFT for Phonon Dispersion Calculations. For phonon dispersion calculations, to avoid imaginary frequencies by PBE functional for Ge doped cases, the total energies and relaxed geometries were calculated by DFT within the local density approximation (LDA) with ultra-soft pseudopotentials.[50, 53, 54] The total energy convergence criterion, and basis set cutoff energy and *k*-mesh grids are the same as above electronic structure calculations.

To quantitatively explore the origin of the lattice thermal conductivity at the atomic level, we used the Debye-Callaway model[55] to numerically evaluate the lattice thermal conductivity of Ge-alloyed PbSe. It is known that the relationship between phonon frequency and crystal volume change is characterized by Grüneisen parameters, which allow us to estimate the lattice anharmonicity and better understand the physical nature of lattice thermal conductivity. We calculated the phonon and Grüneisen dispersions within the quasi-harmonic approximation. The phonon dispersions are calculated on a 128 atoms cell at two volumes, one being the equilibrium volume V_0 and the other being the isotropically compressed volume $0.98V_0$.

The Debye-Callaway formalism[55] has been shown to produce accurate values of lattice thermal conductivity, compared to experiment, for low-conductivity thermoelectric compounds.[56-60] The total lattice thermal conductivity can be written as a sum over one longitudinal κ_{LA} and two transverse κ_{TA} and $\kappa_{TA'}$ acoustic phonon branches: $\kappa_{lat} = \kappa_{LA} + \kappa_{TA} + \kappa_{TA'}$. The partial conductivities κ_i (*i* corresponds to *LA, TA*, and *TA′* modes) are given by:

$$\kappa_i = \frac{1}{3} C_i T^3 \left\{ \int_0^{\Theta_i/T} \frac{\tau_c^i(x) x^4 e^x}{(e^x-1)^2} dx + \frac{\left[\int_0^{\Theta_i/T} \frac{\tau_c^i(x) x^4 e^x}{\tau_N^i (e^x-1)^2} dx \right]^2}{\int_0^{\Theta_i/T} \frac{\tau_c^i(x) x^4 e^x}{\tau_N^i \tau_U^i (e^x-1)^2} dx} \right\} \quad (1)$$

In this expression, Θ_i is the longitudinal (transverse) Debye temperature, $1/\tau_N^i$ is the scattering rate for normal phonon processes, $1/\tau_R^i$ is the sum of all resistive scattering processes, and $1/\tau_c^i = 1/\tau_N^i + 1/\tau_R^i$, $x = \hbar\omega/k_B T$, and $C_i = k_B^4/2\pi^2\hbar^3 v_i$, here, $\hbar$ is the Planck constant, k_B is the Boltzmann constant, ω is the phonon frequency, and v_i is the longitudinal or transverse acoustic phonon velocity. All these scattering processes are

considered for acoustic phonon modes only.

In our case, the resistive scattering rate includes the scattering rates due to Umklapp phonon-phonon scattering ($1/\tau_U^i$), and normal phonon scattering ($1/\tau_N^i$). The normal phonon scattering and Umklapp can be written as,

$$\frac{1}{\tau_N^{LA}(x)} = \frac{k_B^5 \gamma_{LA}^2 V}{M\hbar^4 v_{LA}^5} x^2 T^5 \quad (2)$$

$$\frac{1}{\tau_N^{TA/TA'}(x)} = \frac{k_B^5 \gamma_{TA/TA'}^2 V}{M\hbar^4 v_{TA/TA'}^5} x T^5 \quad (3)$$

$$\frac{1}{\tau_U^i(x)} = \frac{k_B^2 \gamma_i^2}{M\hbar v_i^2 \Theta_i} x^2 T^3 e^{-\theta_i/3T} \quad (4)$$

where γ, V, and M are the Grüneisen parameter, the volume per atom, and the average mass of an atom in the crystal, respectively. The Grüneisen parameter can be defined as, $\gamma_i = -\frac{V\partial\omega_i}{\omega_i \partial V}$, characterizing the relationship between phonon frequency and volume change.

3. RESULTS AND DISCUSSION

Samples with the compositions of $Pb_{0.9955}Sb_{0.0045}Se$-x%GeSe (x = 0, 3, 6, 9, 12 and 14) were synthesized by a vacuum melting method as described in the experimental section. Then the samples were ground and SPS processed followed by annealing at 923 K for over 5 h and subsequent cooling to room temperature in 5 h, and this annealing treatment was repeated thrice. The Sb was used as n-type dopant to control the carrier concentration *n*. The doping amount of 0.45% Sb gives *n* in the range of 2.9 to 5.6 × 10^{19} cm^{-3}.

Structural Characterization and Optical Properties. The PXRD patterns of $Pb_{0.9955}Sb_{0.0045}Se$-x%GeSe show a good match to the PbSe cubic phase with a space group of $Fm\bar{3}m$ (JCPDS # 06-0354), Figures 1a and S1 (Supporting Information). Despite the high substitution levels of up to 14% GeSe, no Ge associated secondary phase or impurity was detected within the PXRD detection limit. The refined lattice parameters decrease with increasing GeSe fraction from 3% to 12% due to the smaller atomic radius of Ge^{2+} (~0.65 Å) compared to Pb^{2+} (~1.20 Å), and confirms the substitution of Pb with Ge in the lattice. However, when the GeSe fraction is > 12%, the lattice parameter deviates from the Vegard's law fitting (red dashed line in Figure 1a), signifying that the solid solution limit of GeSe is around 12%. The energy band gaps of PbSe-x%GeSe samples increase systematically with

increasing GeSe fraction, Figure 1b. From ~0.20 eV of the pure PbSe sample, the band gap shifts to ~0.25 eV for the 3% GeSe alloy then saturates near 0.28 eV for the samples with ≥ 6% GeSe content. These results are consistent with the larger band gap value of GeSe (*i.e.* 1.14 eV).[61]

Charge Transport Properties.

All samples show negative Hall coefficients, indicating that electrons are the majority charge carriers, Figures 2a and 2d. Interestingly, as the GeSe fraction increases to 12%, the Hall coefficient becomes more negative, indicating fewer charge carriers in the system. This is unexpected given the level of Sb n-type dopant is constant. The origin of this effect may lie in possible interactions of the GeSe fraction with Sb essentially deactivating its donor behavior. The 14% GeSe containing sample (in which the GeSe solubility limit is exceeded)) is an exception in the R_H and n trends likely because of pronounced precipitated phase within the PbSe matrix, evidence of which is observed in TEM studies of the 12% GeSe sample (see below).

The Hall coefficients and carrier concentrations (Figure 2b) are nearly independent of the temperature. It is evident that the solid solution of GeSe alloyed $Pb_{0.9955}Sb_{0.0045}Se$ drastically reduces the carrier mobility with respect to the control composition $Pb_{0.9955}Sb_{0.0045}Se$, but this effect appears to be nearly saturated for samples with x ≥ 6, Figure 2c. According to the power law of $\mu \propto T^{-r}$ in $Pb_{0.9955}Sb_{0.0045}Se$ the r value is ~3/2, which indicates the electronic scattering is dominated by acoustic phonons over the whole temperature range. For the GeSe alloyed samples, the r value is ~1/2 from 300 K to ~550 K then increases to ~2 above 550 K. The r ~1/2 may be attributed typically attributed to electronic scattering by optical phonons but could also be a combination of a) electrons interacting with acoustic phonons and b) localized impurities ($r < -1$). The introduction of Ge into the crystal structure can act as a source of both optical modes and impurity scattering centers, so it is difficult to isolate a single mechanism. The increase in r from ~3/2 to ~2 at higher temperatures is attributed to the density of states (DOS) effective mass of the charge carriers becoming heavier as the temperature rises as shown in Figure 6d and Figure S2 (Supporting Information).

Figure 3a shows that the temperature-dependent electrical conductivity of

$Pb_{0.9955}Sb_{0.0045}Se$-x%GeSe samples decreases with increasing x as a result of the simultaneous drops in n and μ_H (Figures 2b and c). The electrical conductivities decrease monotonically from ~4370 Scm^{-1} for $Pb_{0.9955}Sb_{0.0045}Se$ to ~970 Scm^{-1} for $Pb_{0.9955}Sb_{0.0045}Se$-12%GeSe at 300 K. As shown in Figures 2c and 2d, the reduction of the electrical conductivity is mainly attributed to the decrease in n from ~5.6×10^{19} (for x = 0) to ~2.9×10^{19} cm^{-3} (for x = 12) and μ_H from ~487 (for x = 0) to ~197 $cm^2V^{-1}s^{-1}$ (for x = 12). When the temperature rises, the electrical conductivity for all samples declines due to the reduction in μ_H, confirming the degenerate semiconductor behavior seen in the carrier concentration data.

The Seebeck coefficients as a function of temperature for $Pb_{0.9955}Sb_{0.0045}Se$-x%GeSe are presented in Figure 3b. The negative signs of the Seebeck coefficients indicate the n-type nature of the samples and is consistent with the negative values of the Hall coefficients (Figures 2a and d). In general, the magnitudes of the Seebeck coefficients rise upon alloying with GeSe, and all samples exhibit a mainly linear S vs. T trend. At 300 K, the absolute values of the Seebeck coefficient increase because of the decrease in carrier concertation caused by the higher GeSe fractions. In detail, the values are notably enhanced from −49 (for x = 0) to −80 μVK^{-1} (for x = 14) at 300 K and become larger at increased temperatures. Specifically, the highest values of Seebeck coefficient ~−250 μVK^{-1} for $Pb_{0.9955}Sb_{0.0045}Se$-12%GeSe is obtained at 923 K, an enhancement of ~25% compared with that of $Pb_{0.9955}Sb_{0.0045}Se$ (~−200 μVK^{-1}).

The temperature-dependent power factors for $Pb_{0.9955}Sb_{0.0045}Se$-x%GeSe are shown in Figure 3c. Because of its remarkably high electrical conductivity, the $Pb_{0.9955}Sb_{0.0045}Se$ (x=0) sample exhibits the largest power factor in the entire temperature range with the highest value of ~21.0 $\mu Wcm^{-1}K^{-2}$ at 773 K. The $Pb_{0.9955}Sb_{0.0045}Se$-12%GeSe sample shows the second highest value with a maximum power factor of ~19.1 $\mu Wcm^{-1}K^{-2}$ at 623 K.

Figure 3d illustrates the Seebeck coefficient as a function of Hall carrier density (the Pisarenko relation) for $Pb_{0.9955}Sb_{0.0045}Se$-x%GeSe at 296 K. The solid curves are the theoretical calculated values based on the single parabolic band (SPB) model for n-type PbSe with effective mass of electrons of 0.3 m_e, 0.35 m_e and 0.4 m_e (m_e is the free electron mass).

The $Pb_{0.9955}Sb_{0.0045}Se$-14%GeSe sample has the highest electron effective mass ~0.4 m_e compared to the others. With rising temperature, the effective mass of electrons increases for $Pb_{0.9955}Sb_{0.0045}Se$-x%GeSe (x = 0, 6, 9 and 12) samples (Figure S2, Supporting Information). These experimental data are in excellent agreement with the theoretical values (see below). The decrease of the Seebeck coefficients with higher carrier concentration suggests that single-band transport is the main characteristic of the charge carriers in $Pb_{0.9955}Sb_{0.0045}Se$-x%GeSe.

Thermal Conductivity. The most striking finding in this work is that the introduction of GeSe in the PbSe lattice has profound effects on the reduction of thermal conductivity. For example, at 300 K, the total thermal conductivity value of $Pb_{0.9955}Sb_{0.0045}Se$-12%GeSe (1.52 $Wm^{-1}K^{-1}$) is more than two times lower than that of $Pb_{0.9955}Sb_{0.0045}Se$ (4.69 $Wm^{-1}K^{-1}$). Typical total thermal conductivity values for $Pb_{0.9955}Sb_{0.0045}Se$-x%GeSe as a function of temperature are shown in Figure 4a. For samples with x < 12, the thermal conductivity continuously decreases at increased temperatures, while a slight rise occurs at T > 800 K for samples with x = 12 and 14. The GeSe-alloyed samples exhibit remarkably reduced thermal conductivity compared to $Pb_{0.9955}Sb_{0.0045}Se$ in the measured temperature range. In order to better investigate the significant reduction of the total thermal conductivity, we evaluated the contribution of the lattice thermal conductivity (κ_{lat}) and free-carrier thermal conductivity (κ_{ele}).

The κ_{ele} was estimated using the Wiedemann-Franz relation, $\kappa_{ele} = L\sigma T$, where σ is the electrical conductivity, T is the absolute temperature, and L is the Lorenz number, which was estimated using the equation:[62]

$$L = 1.5 + \exp[-|S|/116] \times 10^{-8}\ V^2K^{-2} \quad (1)$$

Figures S2a and S2d (Supporting Information) shows the resulting Lorenz numbers and κ_{ele}.

The room temperature κ_{lat} (Figure 4b), decreases by 50% from ~1.84 $Wm^{-1}K^{-1}$ for $Pb_{0.9955}Sb_{0.0045}Se$ to ~0.96 $Wm^{-1}K^{-1}$ for $Pb_{0.9955}Sb_{0.0045}Se$-14%GeSe. Surprisingly, the κ_{lat} achieves an extremely low value of ~0.36 $Wm^{-1}K^{-1}$ at 573 K for $Pb_{0.9955}Sb_{0.0045}Se$-12%GeSe. It is worth noting that this is close to the theoretical minimum of ~0.38 $Wm^{-1}K^{-1}$ for PbSe and therefore we refer to the estimated value of ~0.36 $Wm^{-1}K^{-1}$ at 573 K for

$Pb_{0.9955}Sb_{0.0045}Se$-12%GeSe as ultralow[63] and it is in the same order of other know ultralow thermal conductivity materials such as SnSe[64-66] and $CsAg_5Te_3$.[58] The rise of κ_{lat} at $T > 600$ K is likely due to the increased contribution of bipolar diffusion of minority carriers that is not accounted for exactly by the Lorenz number.

Microstructure Analysis. To understand the remarkably strong phonon scattering mechanisms operating in this system, we carried out S/TEM structural analysis of $Pb_{0.9955}Sb_{0.0045}Se$-12%GeSe and performed first-principles calculations to obtain insights into the phonon properties, as detailed in the following sections. The microstructure of $Pb_{0.9955}Sb_{0.0045}Se$-12%GeSe was investigated with scanning/transmission electron microscopy (S/TEM). Sparse nanoscale precipitates, which are rich in Ge and deficient in Pb and Se were observed, as shown in Figures 5a and 5b. The precipitates have a semi-coherent interface with the matrix as shown in Figure 5d. It is worth noting that these nanoscale precipitates are observed only in some of the grains being examined with TEM, which means that most of the GeSe has dissolved into the matrix to form a solid solution. Decent numbers of dislocations aligned in certain directions were also observed in some of the grains and at grain boundaries in this material, Figures 5e and 5f. The selected area diffraction (SAED) pattern taken along the [111] zone axis within the area shown in Figure 5e matches the rock-salt (NaCl) structure. No diffraction spot splitting or additional spots, were observed in the SAED pattern. Thus, the sample is mostly in the form of a solid solution.

DFT Calculations. We explored the electronic band structure modifications of PbSe by alloying with GeSe using first-principles density functional theory (DFT) calculations. Considering that the dopant Sb atoms only serve to control the carrier concentration, we do not include Sb atoms for simplicity of the calculations. It is shown in Figures 6a and 6b, that when Ge atoms are added into PbSe, both the conduction band minimum (CBM) and valence band maximum (VBM) at the L point move away from the Fermi level, which leads to an enlarged band gap. In addition, as the CBM and VBM at L point change faster than those at Σ point, $\Delta E_{L-\Sigma}$ decreases for both conduction and valence bands.

Note that the above band structure calculations are based on an energetically more favorable configuration where the Ge atoms are distorted off-center from the proper

octahedral position (off). In other words, the Ge atom is shifted away from the regular site (rs) along the <111> direction by about 0.3 Å. Figure 6c shows an energy profile of GeSe-alloyed PbSe as a function of Ge displacement from the octahedral center. The total energy of the system with the Ge atom off-centered from the ideal octahedral site is significantly lowered. This is expected based on the strong tendency of the Ge^{2+} $4s^2$ lone pair of electrons to stereochemically express itself and occupy space. This same tendency is responsible for the compounds GeSe and GeTe to adopt distorted structures and avoid the rock salt NaCl structure type.

To understand the physical reasons for the off-center behavior of Ge in PbSe, we performed crystal orbital Hamiltonian populations (COHP) analysis between Ge and Se electronic states as an indicator of trends in lone-pair stereochemical activity.[67-69] The COHP is the density of states weighted by the corresponding Hamiltonian matrix element and is indicative of the strength and nature of bonding (positive COHP values) or anti-bonding (negative COHP values) interactions. According to the DOS shown in Figure 7, for both the regular undistorted (Figure 7a) and the distorted off-center configurations (Figure 7b), there are mainly strong interactions of Ge4s-Se4p and Ge4p-Se4p in the valence bands. The COHP results (Figure 7c) show that the strong interactions between Ge4s and Se4p are bonding in nature below the Fermi level with the off-center configuration having larger COHP positive values than those of the regular case. Interestingly, the strong interactions between Ge4p and Se4p (Figure 7d) are anti-bonding from −5 to −1.8 eV with the off-center model having less negative values, suggesting that the off-center configuration is less unfavorable than the on-center case. On the other hand there are bonding interactions from −1.8 to −0.2 eV with the off-center case having larger positive values, implying more favorable bonding than the regular case. In other words, with the Ge off-center distortion, the bonding interactions of Ge4s-Se4p and Ge4p-Se4p become stronger and the anti-bonding interaction of Ge4p-Se4p become weaker than the ideal on-center case. Knowing that the anti-bonding interactions destabilize the solid and bonding interactions stabilize it, we thus understand the driving force behind the tendency of Ge to move off center in the PbSe structure. A corollary to this is that the potential energy surface profile around the Ge atoms is a multiple well type based on

which 111 direction it moves. Therefore, thermal energy could shift the Ge atoms from one well to the other in a dynamic fashion causing an incoherent "rattling" motion. This effect has strong consequences in thermal scattering.

To explain the strong lattice thermal conductivity decrease in PbSe, we calculated two sets of phonon vibrations, one for pure PbSe and the other one for GeSe-alloyed PbSe (both with a 128-atoms cell). By comparing the phonon dispersions of the two models (Figure 8a and Figure S4a, Supporting Information), we find that the longitudinal Debye temperature and phonon velocity of the GeSe-alloyed case are all lower than those in PbSe itself. Specifically, the average longitudinal Debye temperature of pure PbSe is around 65 K, while the Ge alloyed PbSe is only 39 K. The average phonon velocity of pure PbSe is 2614 m/s, while the GeSe-alloyed case is decreased to ~2300 m/s. Clearly, the decrease of all these parameters originates in the low frequency "rattling" vibrations of Ge, as shown in the projected phonon density of states (PDOS) (Figure 8b and Figure S4b, Supporting Information).

The calculated lattice thermal conductivity of the two cases and the results are plotted in Figure 8c. As can be seen, the single Ge alloying decreases the thermal conductivity by ~0.6 $Wm^{-1}K^{-1}$ at 300 K and by ~0.3 $Wm^{-1}K^{-1}$ at 900 K. Interestingly, the lone pair induced the off-centering of Ge, which performs very low frequency vibrations is expressed as softened optical modes, Figure 8d. Furthermore, the strong attraction of Ge to the nearest three Se atoms induces longer bonds between these Se atoms and the next nearest (NN) neighbor Pb atoms to which they are bonded. The enlarged Pb coordination environment of these next nearest neighbors results in many new lower frequency vibrations. This is reflected in the PDOS shift to low frequencies relative to those of Pb atoms that are residing farther away from Ge atom (not nearest neighbors). Therefore, the single off-centered Ge atom not only exhibits softened optical vibrations, but also creates a defect induced local strain field that has a strong influence on the next nearest neighbor Pb atoms so that they can engage in lower frequency vibrations. All these effects synergistically contribute to the remarkably lower lattice thermal conductivities observed. Furthermore, the off-centering of the Ge atom is key in the reduction, as mass fluctuation effects due to the alloying are much weaker (Figure S5 and surrounding text, Supporting Information).

In using the Debye-Callaway model above, we only considered the normal and Umklapp processes of acoustic modes; we did not take into account the contributions from low frequency optical modes.[70] By taking into account the optical modes contributions, the calculated lattice thermal conductivity could be further decreased and agree more with experimental results.[71] It is necessary to mention that the calculated Grüneisen parameters of pure PbSe and single Ge-alloyed PbSe (not shown) are very similar and hence play a comparable role to the decrease of the lattice thermal conductivity.

Figure of Merit. The temperature-dependent figure of merit, *ZT*, for $Pb_{0.9955}Sb_{0.0045}Se$-x%GeSe is presented in Figure 4c. All the GeSe-containing samples exhibit enhanced *ZT* compared to the pure $Pb_{0.9955}Sb_{0.0045}Se$. The highest *ZT* value of 1.54 at 773 K was obtained for $Pb_{0.9955}Sb_{0.0045}Se$-12%GeSe and it is essentially on par with many top performing n-type PbTe systems. To evaluate the expected thermoelectric device efficiency of $Pb_{0.9955}Sb_{0.0045}Se$-12%GeSe, the ZT_{avg} was calculated by the following relationship,

$$ZT_{\mathrm{avg}} = \frac{1}{T_{\mathrm{H}} - T_{\mathrm{C}}} \int_{T_{\mathrm{C}}}^{T_{\mathrm{H}}} ZT \mathrm{dT} \qquad (2)$$

where T_h and T_c are the hot- and cold-side temperature, respectively. The ZT_{avg} of ~1.06 between T_c = 400 K and T_h = 800 K is obtained for $Pb_{0.9955}Sb_{0.0045}Se$-12%GeSe, Figure 9b. A comparison of the ZT_{avg} values of $Pb_{0.9955}Sb_{0.0045}Se$-12%GeSe in the present study with those in previous studies on PbSe-based thermoelectric materials is displayed in Figure 9b and Figure S7 (Supporting Information).[4, 8, 20, 33, 34, 37, 39, 41, 42] This ZT_{avg} value is the highest achieved so far for both n- and p-type PbSe-based thermoelectric materials. Furthermore, this value is as good as or even better than that the top n-type PbTe materials.[72-77] This comes despite the lower L conduction band degeneracy relevant to the n-type samples than the L+Σ valence band degeneracy of the p-type counterparts.

4. CONCLUSIONS

The Ge placement on the Pb site of PbSe causes an ultralow lattice thermal conductivity of ~0.36 $Wm^{-1}K^{-1}$ at 573 K for $Pb_{0.9955}Sb_{0.0045}Se$-12%GeSe. First-principles studies suggest that the alloyed Ge atom is off-centered in the lattice and not only exhibits low frequency optical vibrations, but also causes the next nearest neighbor Pb atoms to perform lower frequency oscillations that lead to a softening of the phonon modes. As a result very high thermoelectric

performance can be achieved in n-type selenides $Pb_{0.9955}Sb_{0.0045}Se$-x%GeSe (x = 0, 3, 6, 9, 12 and 14). The GeSe alloying also enlarges the band gap of the PbSe matrix while at the same time allows the retention of the high power factors of n-type PbSe itself. Thus, a high peak *ZT* value of 1.54 at 773 K and a broad temperature plateau of $ZT > 1.2$ from 623 K to 923 K can be realized in $Pb_{0.9955}Sb_{0.0045}Se$-12%GeSe. For n-type PbSe materials this is a top value and matches or exceeds even those reported for n-type PbTe samples. Moreover, with the highest reported ZT_{avg} of 1.06 found from 400 K to 800 K the $Pb_{0.9955}Sb_{0.0045}Se$-12%GeSe composition is an excellent tellurium-free candidate for intermediate-temperature thermoelectric applications.

Author contribution

Z. L., Q. Y and M. G. K. conceived of and planned the experiments. Z. L. prepared the samples and carried out thermoelectric experiments. X. Z., S. C. and V. P. D. conducted TEM measurement of the samples. S. H., X. H. and C. W. carried out the DFT calculations. T. P. B., R. M., and C. U. carried out the Hall measurements. Z. L., G. T., Q. Y., and M. G. K. interpreted all results and wrote and edited the manuscript. All authors have reviewed, discussed and approved the results and conclusions of this article.

Conflicts of interest

There are no conflicts to declare.

Acknowledgements

This work was supported by the Department of Energy, Office of Science Basic Energy Sciences under grant DE-SC0014520, DOE Office of Science (sample preparation, synthesis, XRD, TE measurements, TEM measurements, DFT calculations). ZZL and QY gratefully acknowledge National Natural Science Foundation of China (61728401). This work made use of the EPIC facilities of Northwestern's NUANCE Center, which has received support from the Soft and Hybrid Nanotechnology Experimental (SHyNE) Resource (NSF ECCS-1542205); the MRSEC program (NSF DMR-1121262) at the Materials Research Center; the International Institute for Nanotechnology (IIN); the Keck Foundation; and the State of Illinois, through the IIN. User Facilities are supported by the Office of Science of the

U.S. Department of Energy under Contract No. DE-AC02-06CH11357 and DE-AC02-05CH11231. Access to facilities of high performance computational resources at the Northwestern University is acknowledged. The authors also acknowledge Singapore MOE AcRF Tier 1 under Grant Nos. 2016-T1-002-065, Singapore A*STAR Pharos Program SERC 1527200022, the support from FACTs of Nanyang Technological University for sample analysis.

Supporting Information

Electronic Supplementary Information (ESI) available: PXRD patterns, the Pisarenko relation for $Pb_{0.9955}Sb_{0.0045}Se$-x%GeSe (x = 0, 6, 9 and 12) samples at 296 K, 573 K and 773 K. temperature-dependence Lorenz numbers, thermal diffusivity, heat capacity, electronic thermal conductivity of $Pb_{0.9955}Sb_{0.0045}Se$-12%GeSe (x = 0, 3, 6, 9, 12 and 14), phonon dispersion curves and the projected phonon density of states (PDOS) for pure PbSe, lattice thermal conductivity comparison of pure PbSe and with 5% and 10% Ge alloyed samples without accounting for the off-center defect, repeatability of thermoelectric properties for $Pb_{0.9955}Sb_{0.0045}Se$-12%GeSe, comparison of average figure of merit, ZT_{avg}, values from 300 K to 923 K for several n- and p-type PbSe-based thermoelectric materials, and a table of room temperature densities for $Pb_{0.9955}Sb_{0.0045}Se$-x%GeSe (x = 0, 3, 6, 9, 12 and 14). This material is available free of charge via the Internet at http://pubs.acs.org. See DOI: 10.1039/x0xx00000x

References

1. K. F. Hsu, S. Loo, F. Guo, W. Chen, J. S. Dyck, C. Uher, T. Hogan, E. K. Polychroniadis and M. G. Kanatzidis, *Science*, 2004, **303**, 818-821.
2. Y. Pei, X. Shi, A. LaLonde, H. Wang, L. Chen and G. J. Snyder, *Nature*, 2011, **473**, 66-69.
3. L. D. Zhao, H. J. Wu, S. Q. Hao, C. I. Wu, X. Y. Zhou, K. Biswas, J. Q. He, T. P. Hogan, C. Uher, C. Wolverton, V. P. Dravid and M. G. Kanatzidis, *Energy Environ. Sci.*, 2013, **6**, 3346.
4. Q. Zhang, F. Cao, W. Liu, K. Lukas, B. Yu, S. Chen, C. Opeil, D. Broido, G. Chen and Z. Ren, *J. Am. Chem. Soc.*, 2012, **134**, 10031-10038.
5. Y. Pei, A. D. LaLonde, N. A. Heinz and G. J. Snyder, *Adv. Eng. Mater.*, 2012, **2**, 670-675.
6. K. Biswas, J. He, Q. Zhang, G. Wang, C. Uher, V. P. Dravid and M. G. Kanatzidis, *Nat. Chem.*, 2011, **3**, 160-166.
7. L.-D. Zhao, J. He, S. Hao, C.-I. Wu, T. P. Hogan, C. Wolverton, V. P. Dravid and M. G. Kanatzidis, *J. Am. Chem. Soc.*, 2012, **134**, 16327-16336.
8. L.-D. Zhao, S. Hao, S.-H. Lo, C.-I. Wu, X. Zhou, Y. Lee, H. Li, K. Biswas, T. P. Hogan, C. Uher, C. Wolverton, V. P. Dravid and M. G. Kanatzidis, *J. Am. Chem. Soc.*, 2013, **135**, 7364-7370.
9. J. He, S. N. Girard, M. G. Kanatzidis and V. P. Dravid, *Adv. Funct. Mater.*, 2010, **20**, 764-772.
10. J. P. Heremans, V. Jovovic, E. S. Toberer, A. Saramat, K. Kurosaki, A. Charoenphakdee, S. Yamanaka and G. J. Snyder, *Science*, 2008, **321**, 554-557.
11. Q. Zhang, B. Liao, Y. Lan, K. Lukas, W. Liu, K. Esfarjani, C. Opeil, D. Broido, G. Chen and Z. Ren, *Proc. Natl. Acad. Sci. U.S.A.*, 2013, **110**, 13261-13266.
12. K. Ahn, M.-K. Han, J. He, J. Androulakis, S. Ballikaya, C. Uher, V. P. Dravid and M. G. Kanatzidis, *J. Am. Chem. Soc.*, 2010, **132**, 5227-5235.
13. J. P. Heremans, B. Wiendlocha and A. M. Chamoire, *Energy Environ. Sci.*, 2012, **5**, 5510-5530.
14. J. He, M. G. Kanatzidis and V. P. Dravid, *Materials Today*, 2013, **16**, 166-176.
15. M. G. Kanatzidis, *Chem. Mater.*, 2010, **22**, 648-659.
16. K. Biswas, J. He, I. D. Blum, C.-I. Wu, T. P. Hogan, D. N. Seidman, V. P. Dravid and M. G. Kanatzidis, *Nature*, 2012, **489**, 414-418.
17. S. Johnsen, J. He, J. Androulakis, V. P. Dravid, I. Todorov, D. Y. Chung and M. G. Kanatzidis, *J. Am. Chem. Soc.*, 2011, **133**, 3460-3470.
18. S. N. Girard, J. He, X. Zhou, D. Shoemaker, C. M. Jaworski, C. Uher, V. P. Dravid, J. P. Heremans and M. G. Kanatzidis, *J. Am. Chem. Soc.*, 2011, **133**, 16588-16597.
19. J. He, S. N. Girard, J.-C. Zheng, L. Zhao, M. G. Kanatzidis and V. P. Dravid, *Adv. Mater.*, 2012, **24**, 4440-4444.
20. Y. Lee, S.-H. Lo, J. Androulakis, C.-I. Wu, L.-D. Zhao, D.-Y. Chung, T. P. Hogan, V. P. Dravid and M. G. Kanatzidis, *J. Am. Chem. Soc.*, 2013, **135**, 5152-5160.
21. B. A. Cook, M. J. Kramer, J. L. Harringa, M.-K. Han, D.-Y. Chung and M. G. Kanatzidis, *Adv. Funct. Mater.*, 2009, **19**, 1254-1259.
22. J. Androulakis, C.-H. Lin, H.-J. Kong, C. Uher, C.-I. Wu, T. Hogan, B. A. Cook, T. Caillat, K. M. Paraskevopoulos and M. G. Kanatzidis, *J. Am. Chem. Soc.*, 2007, **129**, 9780-9788.
23. E. M. Levin, B. A. Cook, K. Ahn, M. G. Kanatzidis and K. Schmidt-Rohr, *Phys. Rev. B*, 2009, **80**, 115211.
24. T. Zhu, Y. Liu, C. Fu, J. P. Heremans, J. G. Snyder and X. Zhao, *Adv. Mater.*, 2017, **29**. 1605884.

25. A. S. Rattner and S. Garimella, *Energy*, 2011, **36**, 6172-6183.
26. L.-D. Zhao, V. P. Dravid and M. G. Kanatzidis, *Energy Environ. Sci.*, 2014, **7**, 251-268.
27. Y. Pei, H. Wang and G. J. Snyder, *Adv. Mater.*, 2012, **24**, 6125-6135.
28. Z. Hu and S. Gao, *Chem. Geol.*, 2008, **253**, 205-221.
29. H. Sitter, K. Lischka and H. Heinrich, *Phys. Rev. B*, 1977, **16**, 680-687.
30. D. Parker and D. J. Singh, *Phys. Rev. B*, 2010, **82**, 035204.
31. H. Wang, Y. Pei, A. D. LaLonde and G. J. Snyder, *Adv. Mater.*, 2011, **23**, 1366-1370.
32. T. C. Chasapis, Y. Lee, E. Hatzikraniotis, K. M. Paraskevopoulos, H. Chi, C. Uher and M. G. Kanatzidis, *Phys. Rev. B*, 2015, **91**, 085207.
33. J. Androulakis, I. Todorov, J. He, D.-Y. Chung, V. Dravid and M. Kanatzidis, *J. Am. Chem. Soc.*, 2011, **133**, 10920-10927.
34. Q. Zhang, H. Wang, W. Liu, H. Wang, B. Yu, Q. Zhang, Z. Tian, G. Ni, S. Lee, K. Esfarjani, G. Chen and Z. Ren, *Energy Environ. Sci.*, 2012, **5**, 5246-5251.
35. H. Wang, Y. Pei, A. D. LaLonde and G. J. Snyder, *Proc. Natl. Acad. Sci. U.S.A.*, 2012, **109**, 9705-9709.
36. S. Hao, F. Shi, V. P. Dravid, M. G. Kanatzidis and C. Wolverton, *Chem. Mater.*, 2016, **28**, 3218-3226.
37. C.-F. Wu, T.-R. Wei, F.-H. Sun and J.-F. Li, *Adv. Sci.*, 2017, **4**, 1700199.
38. Z. Chen, B. Ge, W. Li, S. Lin, J. Shen, Y. Chang, R. Hanus, G. J. Snyder and Y. Pei, *Nat. Commun.*, 2017, **8**, 13828.
39. Y. Lee, S. H. Lo, C. Chen, H. Sun, D. Y. Chung, T. C. Chasapis, C. Uher, V. P. Dravid and M. G. Kanatzidis, *Nat. Commun.*, 2014, **5**, 3640.
40. L. Fu, M. Yin, D. Wu, W. Li, D. Feng, L. Huang and J. He, *Energy Environ. Sci.*, 2017, **10**, 2030.
41. H. Wang, Z. M. Gibbs, Y. Takagiwa and G. J. Snyder, *Energy Environ. Sci.*, 2014, **7**, 804-811.
42. W. Shanyu, Z. Gang, L. Tingting, S. Xiaoyu, L. Han and T. Xinfeng, *J. Phys. D: Appl. Phys.*, 2011, **44**, 475304.
43. T. J. McCarthy, S. P. Ngeyi, J. H. Liao, D. C. DeGroot, T. Hogan, C. R. Kannewurf and M. G. Kanatzidis, *Chem. Mater.*, 1993, **5**, 331-340.
44. K. A. Borup, J. de Boor, H. Wang, F. Drymiotis, F. Gascoin, X. Shi, L. Chen, M. I. Fedorov, E. Muller, B. B. Iversen and G. J. Snyder, *Energy Environ. Sci.*, 2015, **8**, 423-435.
45. R. Blachnik and R. Igel, *Zeitschrift fur Naturforschung B*, 1974, **29**, 625–629.
46. P. Hohenberg and W. Kohn, *Phys. Rev.*, 1964, **136**, B864-B871.
47. W. Kohn and L. J. Sham, *Phys. Rev.*, 1965, **140**, A1133-A1138.
48. G. Kresse and J. Hafner, *Phys. Rev. B*, 1993, **47**, 558-561.
49. G. Kresse and J. Hafner, *Phys. Rev. B*, 1994, **49**, 14251-14269.
50. G. Kresse and J. Furthmüller, *Phys. Rev. B*, 1996, **54**, 11169-11186.
51. G. Kresse and J. Furthmüller, *Comput. Mater. Sci.*, 1996, **6**, 15-50.
52. J. P. Perdew, A. Ruzsinszky, G. I. Csonka, O. A. Vydrov, G. E. Scuseria, L. A. Constantin, X. Zhou and K. Burke, *Phys. Rev. Lett.*, 2008, **100**, 136406.
53. J. P. Perdew and A. Zunger, *Phys. Rev. B*, 1981, **23**, 5048-5079.
54. D. Vanderbilt, *Phys. Rev. B*, 1990, **41**, 7892-7895.
55. M. Asen-Palmer, K. Bartkowski, E. Gmelin, M. Cardona, A. P. Zhernov, A. V. Inyushkin, A. Taldenkov, V. I. Ozhogin, K. M. Itoh and E. E. Haller, *Phys. Rev. B*, 1997, **56**, 9431-9447.
56. D. T. Morelli, J. P. Heremans and G. A. Slack, *Phys. Rev. B*, 2002, **66**, 195304.
57. Y. Zhang, E. Skoug, J. Cain, V. Ozoliņš, D. Morelli and C. Wolverton, *Phys. Rev. B*, 2012, **85**, 054306.
58. L. Hua, T. Gangjian, S. Jin-Ni, H. Shiqiang, W. Li-Ming, C. Nicholas, M. Christos, W. Si, U. Ctirad, W.

Christopher and K. M. G., *Angew. Chem. Int. Ed.*, 2016, **55**, 11431-11436.
59. G. Tan, S. Hao, J. Zhao, C. Wolverton and M. G. Kanatzidis, *J. Am. Chem. Soc.*, 2017, **139**, 6467-6473.
60. J. Zhao, S. Hao, S. M. Islam, H. Chen, S. Ma, C. Wolverton and M. G. Kanatzidis, *Inorg. Chem.*, 2018, DOI: 10.1021/acs.inorgchem.8b01383.
61. D. D. Vaughn Ii, R. J. Patel, M. A. Hickner and R. E. Schaak, *J. Am. Chem. Soc.*, 2010, **132**, 15170-15172.
62. H.-S. Kim, Z. M. Gibbs, Y. Tang, H. Wang and G. J. Snyder, *APL Mater.*, 2015, **3**, 041506.
63. D. G. Cahill, S. K. Watson and R. O. Pohl, *Phys. Rev. B*, 1992, **46**, 6131-6140.
64. C. Chang, M. Wu, D. He, Y. Pei, C.-F. Wu, X. Wu, H. Yu, F. Zhu, K. Wang, Y. Chen, L. Huang, J.-F. Li, J. He and L.-D. Zhao, *Science*, 2018, **360**, 778-783.
65. L.-D. Zhao, G. Tan, S. Hao, J. He, Y. Pei, H. Chi, H. Wang, S. Gong, H. Xu, V. P. Dravid, C. Uher, G. J. Snyder, C. Wolverton and M. G. Kanatzidis, *Science*, 2015, **351**, 141-144.
66. L.-D. Zhao, S.-H. Lo, Y. Zhang, H. Sun, G. Tan, C. Uher, C. Wolverton, V. P. Dravid and M. G. Kanatzidis, *Nature*, 2014, **508**, 373.
67. R. Dronskowski and P. E. Bloechl, *J. Phys. Chem.*, 1993, **97**, 8617-8624.
68. U. V. Waghmare, N. A. Spaldin, H. C. Kandpal and R. Seshadri, *Phys. Rev. B*, 2003, **67**, 125111.
69. M. Stefan, D. V. L., T. A. L. and D. Richard, *J. Comput. Chem.*, 2016, **37**, 1030-1035.
70. P. G. Klemens, *Proc. Phys. Soc. A*, 1955, **68**, 1113.
71. P. Ying, X. Li, Y. Wang, J. Yang, C. Fu, W. Zhang, X. Zhao and T. Zhu, *Adv. Funct. Mater.*, 2017, **27**, 1604145.
72. Y. Xiao, H. Wu, W. Li, M. Yin, Y. Pei, Y. Zhang, L. Fu, Y. Chen, S. J. Pennycook, L. Huang, J. He and L.-D. Zhao, *J. Am. Chem. Soc.*, 2017, **139**, 18732-18738.
73. Q. Zhang, Q. Song, X. Wang, J. Sun, Q. Zhu, K. Dahal, X. Lin, F. Cao, J. Zhou, S. Chen, G. Chen, J. Mao and Z. Ren, *Energy Environ. Sci.*, 2018, **11**, 933-940.
74. J. Zhang, D. Wu, D. He, D. Feng, M. Yin, X. Qin and J. He, *Adv. Mater.*, 2017, **29**, 1703148.
75. G. Tan, C. C. Stoumpos, S. Wang, T. P. Bailey, L.-D. Zhao, C. Uher and M. G. Kanatzidis, *Adv. Eng. Mater.*, 2017, **7**, 1700099.
76. L. Fu, M. Yin, D. Wu, W. Li, D. Feng, L. Huang and J. He, *Energy Environ. Sci.*, 2017, **10**, 2030-2040.
77. Z. Chen, B. Ge, W. Li, S. Lin, J. Shen, Y. Chang, R. Hanus, G. J. Snyder and Y. Pei, *Nat. Commun.*, 2017, **8**, 13828.
78. W. Chao- Feng, W. Tian- Ran, S. Fu- Hua and L. Jing- Feng, *Adv. Sci.*, 2017, **4**, 1700199.

Figures:

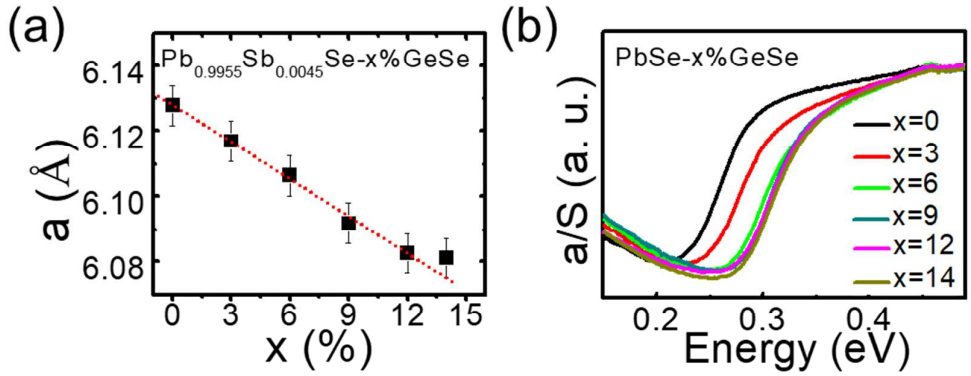

Figure 1. (a) Refined lattice parameters of $Pb_{0.9955}Sb_{0.0045}$Se-x%GeSe as a function of GeSe content, indicating a linear contraction of the lattice from x = 0 to x = 12; (b) Electronic absorption spectra obtained from diffuse reflectance infrared spectroscopy measurements on PbSe-x%GeSe samples (without Sb doping to avoid spectroscopic interference from free carriers), showing the increasing band gap with increasing GeSe content.

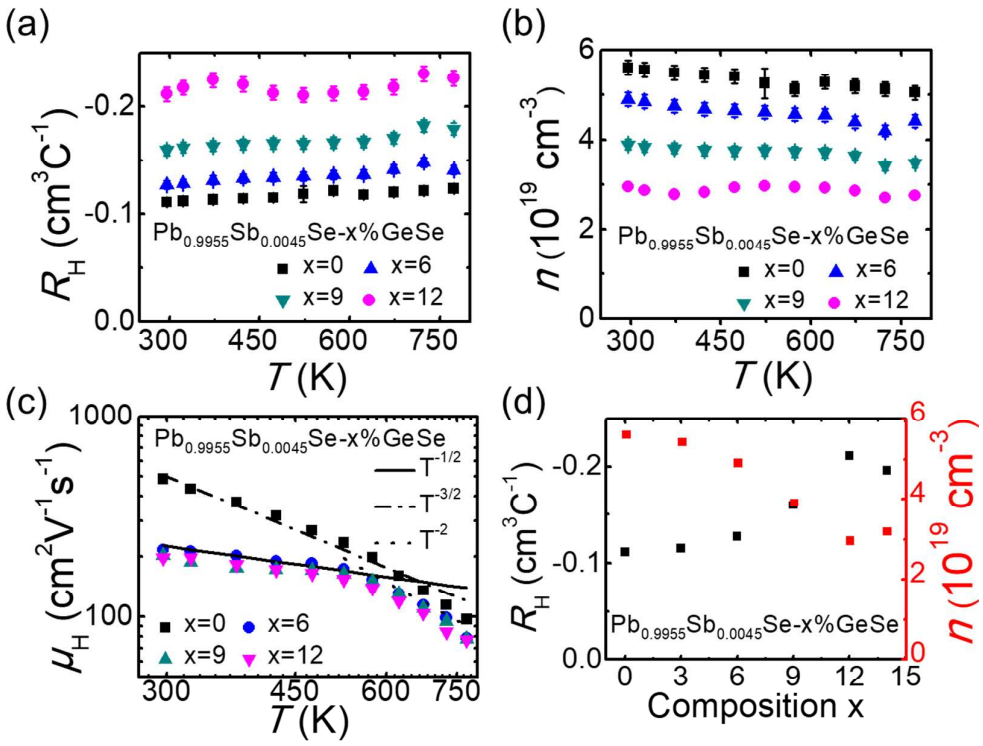

Figure 2. The temperature dependence of (a) the Hall coefficient R_H; (b) carrier concentration n; (c) Hall mobility μ_H, in n-type $Pb_{0.9955}Sb_{0.0045}Se$-x%GeSe (x = 0, 6, 9, 12); and (d) the R_H and n at 296 K for $Pb_{0.9955}Sb_{0.0045}Se$-x%GeSe (x = 0, 3, 6, 9, 12 and 14). The lines in (c) represent the power law behavior expected for different charge carrier scattering mechanisms.

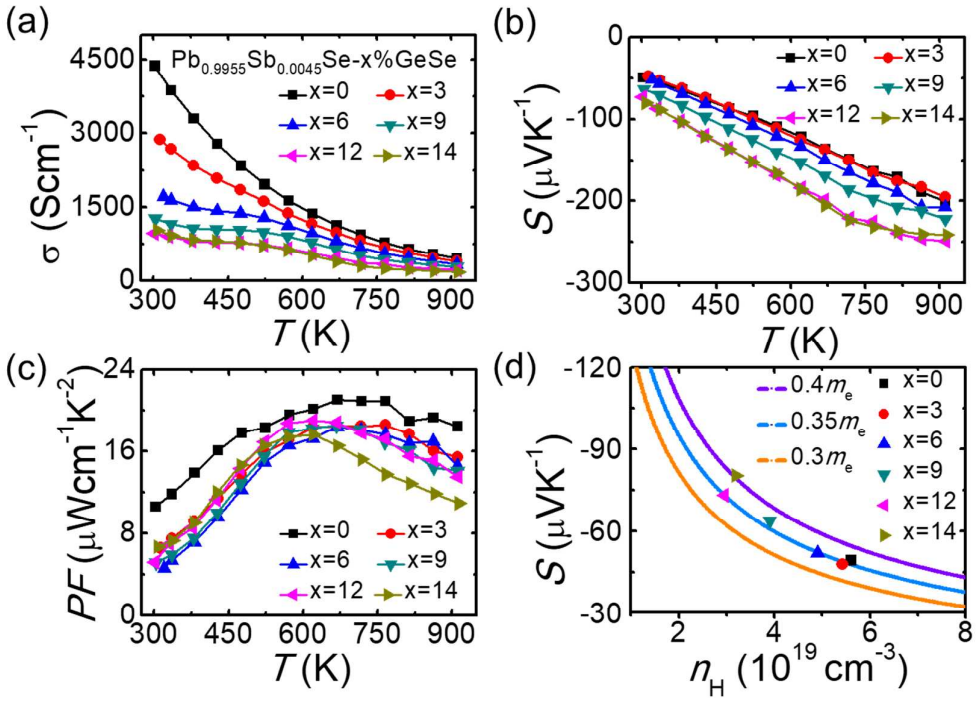

Figure 3. Transport properties as a function of temperature for $Pb_{0.9955}Sb_{0.0045}Se$-x%GeSe SPSed pellets; (a) electrical conductivity, σ; (b) Seebeck coefficient, S; (c) power factor, PF; and (d) Seebeck coefficient as a function of Hall carrier concentration at 296 K. The solid curves in (d) are the theoretical Pisarenko curves for n-type PbSe with effective mass of electrons of 0.3 m_e (orange), 0.35 m_e (cyan) and 0.4 m_e (purple).

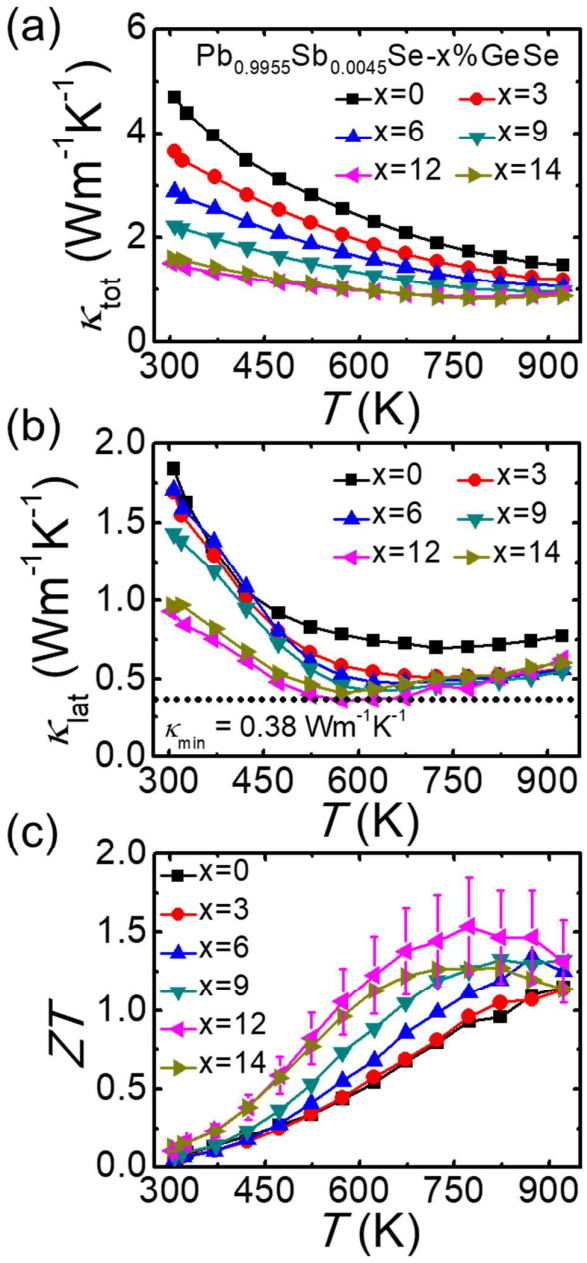

Figure 4. (a) Total thermal conductivity, κ_{tot}; (b) Lattice thermal conductivity, κ_{lat}, with the amorphous limit of PbSe given as a dotted line; and (c) Figure of merit, *ZT,* values for $Pb_{0.9955}Sb_{0.0045}Se$-x%GeSe.

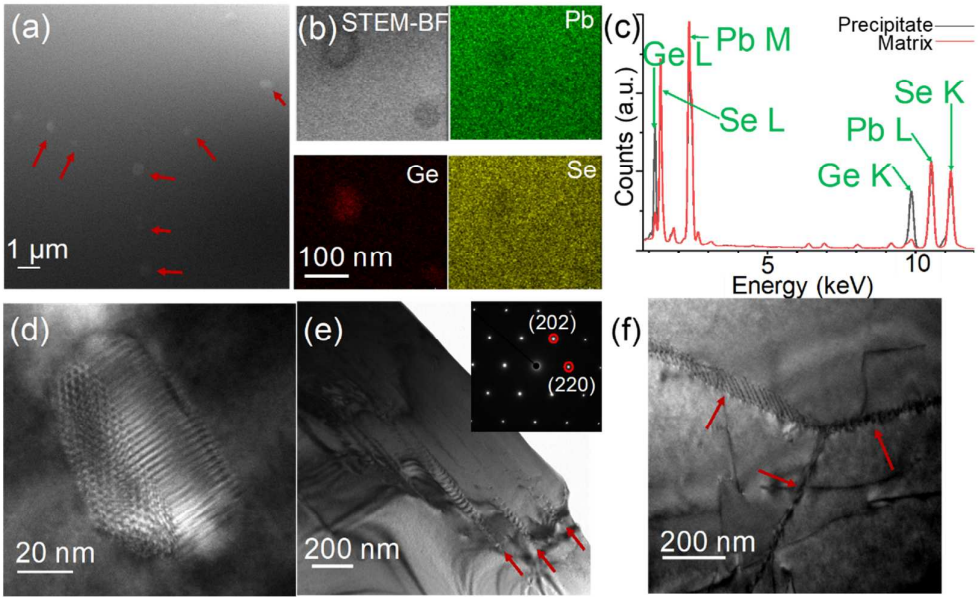

Figure 5. (a) Annular dark field image of n-type $Pb_{0.9955}Sb_{0.0045}Se$–12%GeSe, showing both Z-contrast and diffraction contrast. The nanoscale precipitates are selectively indicated by red arrows; (b) STEM bright field (BF) image and EDS elemental maps of representative nanoscale precipitates. The elemental maps show that these precipitates are rich in Ge and deficient in Pb and Se; (c) EDS spectra taken from precipitate (grey solid line) and matrix (red solid line). The spectra were taken with same conditions (e.g.: acquisition time, collection angle, beam current, spot size, sample thickness, etc.), and the peak intensity of Ge is significantly higher in the precipitate than that in the matrix; (d) Representative high resolution TEM image of the nanoscale precipitates. The Moire fringes indicate misfit or misorientation between the matrix and the precipitate; (e) and (f) Dislocations in grain and at grain boundaries, pointed to by red arrows. The inset in the upper right corner of (e) is the SAED pattern taken within the area of (e) along the [111] zone axis.

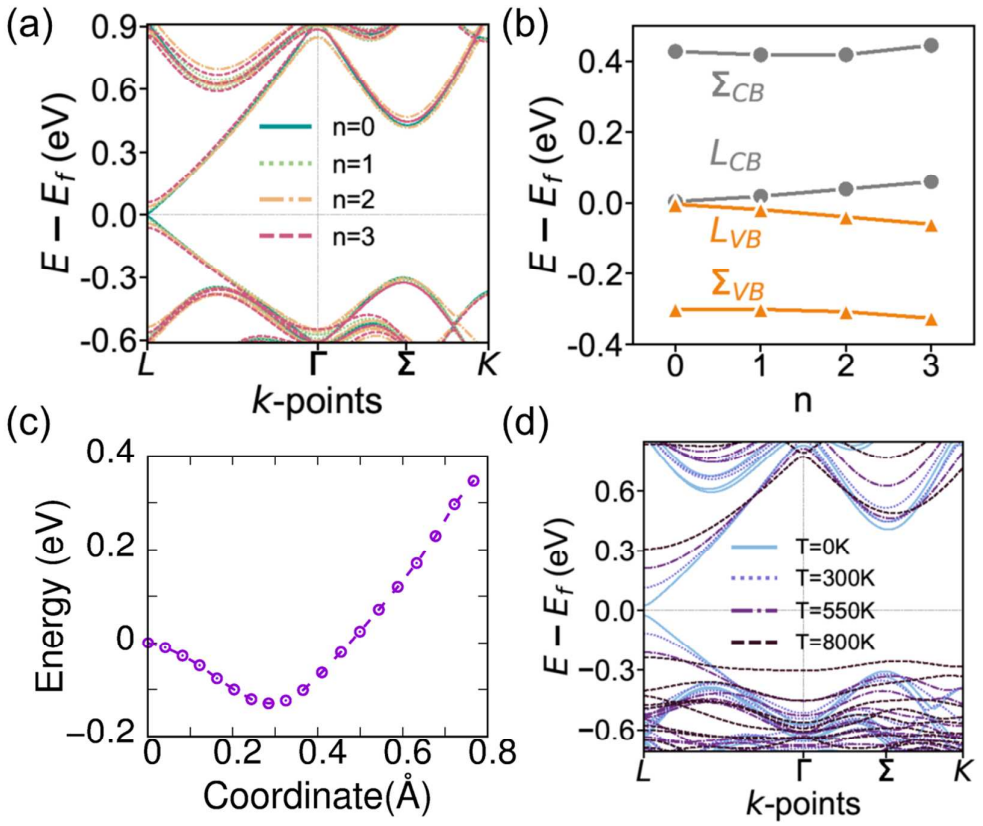

Figure 6. (a) Calculated electronic band structures of off-center GeSe-doped $Pb_{27-n}Ge_nSe_{27}$ (n = 0, 1, 2, and 3) with spin-orbit coupling included; (b) Calculated band-edge energies of the conduction band (CB) and valence band (VB) at L and Σ, as a function of n in $Pb_{27-n}Ge_nSe_{27}$; and (c) The energy profile of GeSe-doped PbSe as a function of coordinates from regular Ge substituted Pb site along <111> direction to the center of tetrahedral site; and (d) Calculated electronic band structures of $Pb_{25}Ge_2Se_{27}$ at T = 0, 300, 550, and 800 K with spin-orbit coupling included.

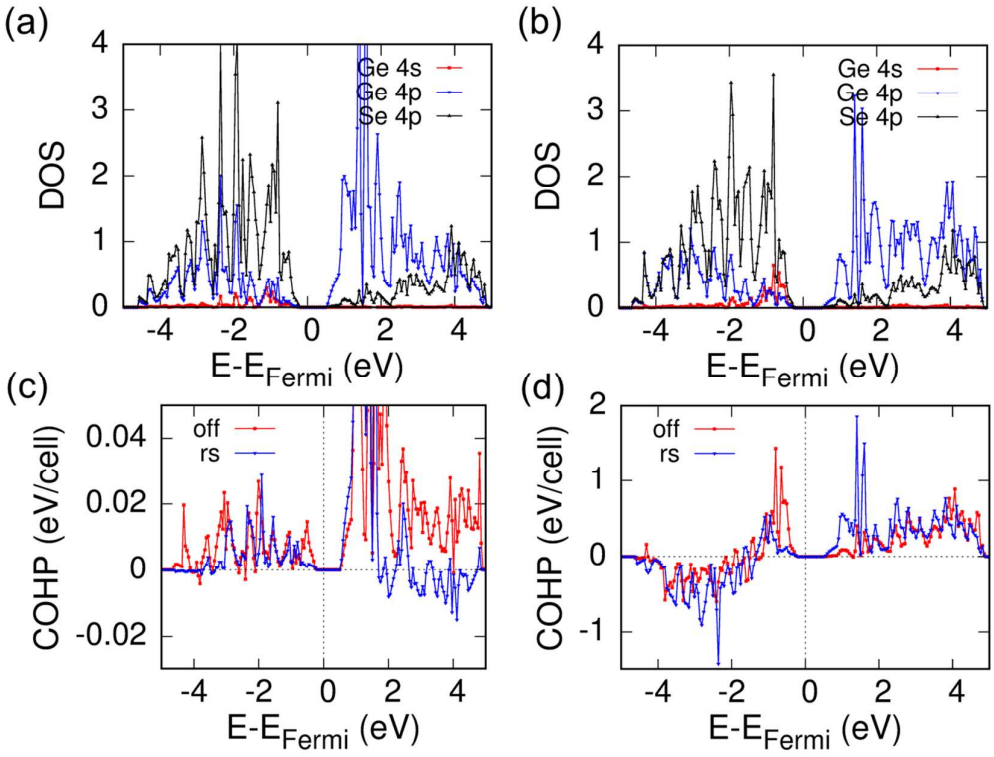

Figure 7. (a) Electronic density of states of Ge 4s, 4p and Se 4p states with (a) Ge in a regular Pb site and (b) Ge in an off-centered position. Crystal orbital Hamiltonian populations (COHP) of (c) Ge4s-Ge4p and (d) Ge4p-Se4p. The positive values of COHP suggest bonding interactions that stabilize the structure and negative COHP values imply anti-bonding interactions that destabilize the structure.

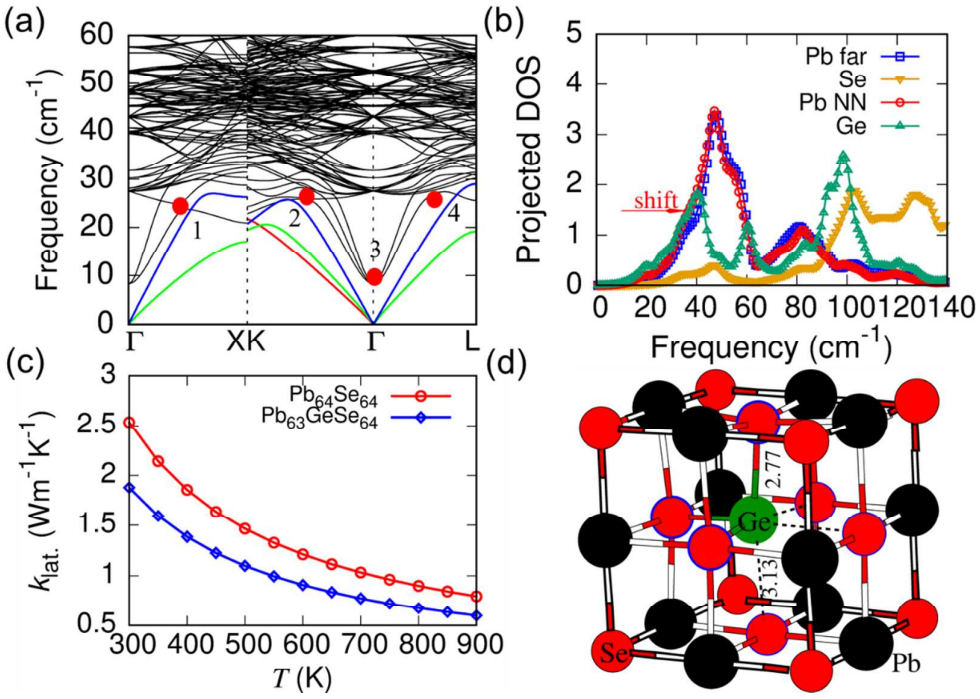

Figure 8. (a) Phonon dispersion curves (red and green for the transverse acoustic branches and blue for the longitudinal); (b) the projected phonon density of states (PDOS) for Ge-alloyed PbSe, "Pb NN" stands for the 6 Pb atoms that are next nearest neighbors to the Ge atom within the supercell, while the remainder of the Pb atoms are denoted as "Pb far"; (c) Comparison of pure PbSe and Ge-alloyed PbSe lattice thermal conductivities as a function of temperature, calculated from the DFT phonon dispersion curves and Debye-Callaway formalism; and (d) Illustration of the Ge off-center structure model with typical bond lengths of Ge-Se and Pb-Se. The distance between the off-center Ge and three nearest Se is 2.77 Å and for the other three pairs, 3.13 Å. The normal bond length of Pb-Se is 3.05 Å and the normal bond length of Ge-Se (*Pnma* structure) within the same layer is 2.60 Å. Thus, the lone pair of Ge itself occupies its own space, performing very low frequency vibrations and soften optical modes. Some interesting vibration models corresponding to the red dots in (a) are included as movies in the Supporting Information.

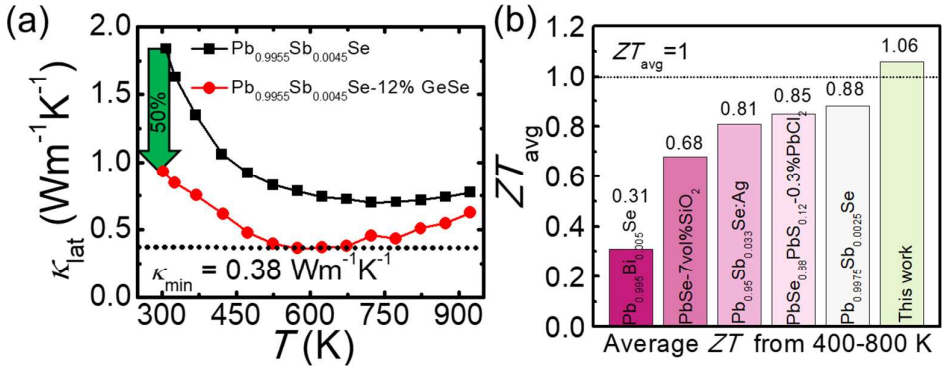

Figure 9. (a) Comparison of lattice thermal conductivity, κ_{lat}, of n-type $Pb_{0.9955}Sb_{0.0045}Se$–12%GeSe and $Pb_{0.9955}Sb_{0.0045}Se$ in the present study and (b) Comparison of average thermoelectric figure of merit, ZT_{avg}, values with the temperature gradient of 400 K to 800 K for n-type PbSe-based thermoelectric materials in the present study with those in previous reports.[39 33, 78, 68]

Table of Contents Entry

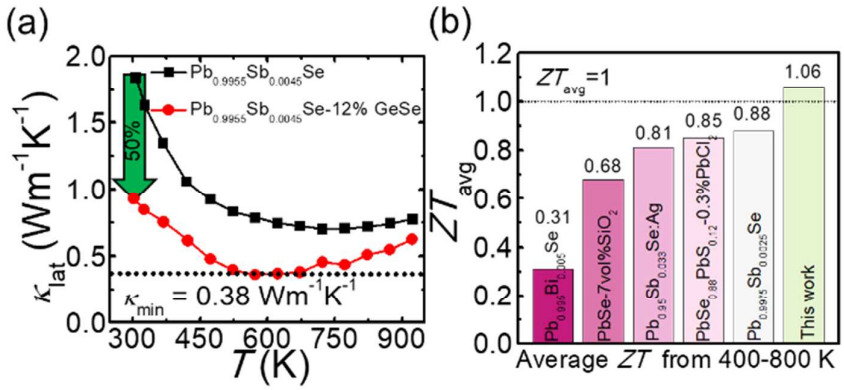

The off-centered Ge leads to the ultralow lattice thermal conductivity and record high average *ZT* for n-type PbSe.

Thermoelectric materials offer the possibility of converting waste heat directly into electricity without moving parts and promise improvements in energy usage and efficiency. Historically PbSe has underperformed PbTe in thermoelectric efficiency and has been regarded as an inferior relative to its telluride congener. However, the fifty-fold greater natural abundance of Se relative to Te makes PbSe much more appealing than PbTe if it could match its performance. This work achieved a high peak ZT of ~1.54 at 773 K for n-type PbSe with a record-high average ZT_{avg} of ~1.06 from 400 K to 800 K, which matches or exceeds those of the best n-type PbTe-based thermoelectric materials. The superior performance is caused mainly by the ultralow thermal conductivity *via* GeSe alloying. The theoretical studies reveal that alloyed Ge^{2+} atoms prefer to stay at off-center lattice positions, inducing very low-frequency optical modesleading to a reduction of the Debye temperature and phonon velocity. The obtained new scientific insights of the role of Ge atoms in PbSe structure will be valuable to design better thermoelectric materials.